Check for updates

Original Article

Institution of MECHANICAL ENGINEERS
Journal of SYSTEMS AND CONTROL ENGINEERING

Proc IMechE Part I:
J Systems and Control Engineering
1–14
© IMechE 2019
Article reuse guidelines:
sagepub.com/journals-permissions
DOI: 10.1177/0959651819854557
journals.sagepub.com/home/pii
SAGE

Reduced order indirect self-tuning regulator for a novel pneumatic tele-operation system

Mohamad Baayoun[1], Naseem Daher[1] and Matthias Liermann[2]

Abstract

This article presents a reduced order indirect self-tuning regulator for a passive pneumatic tele-operation system, which is intended for use in medical surgeries in magnetic resonance imaging environments with short transmission distances ($\approx 10\,m$), where force feedback is required. The novel tele-operation system uses less active components as compared to conventional systems and realizes a bilateral control without the use of a force or pressure sensor. The proposed adaptive control system is validated in simulation and experimentation on a test rig built for this purpose. Special attention is given to the notion of transparency of the system, which is the ratio between the resistance of the master device experienced by the operator and the actual resistance of the remote environment in contact with the slave device. The adaptive controller shows advantage over a previously designed non-adaptive control system design in terms of stiffness, damping, and transparency.

Keywords

Pneumatic actuator, adaptive control, self-tuning regulator, tele-operation, magnetic resonance imaging, transparency

Date received: 27 October 2018; accepted: 4 May 2019

Introduction

Tele-operators are used to allow a human operator to manipulate an object in a remote environment. They are generally composed of master and slave actuators and a communication link in between, as illustrated in Figure 1. Generally, it is assumed that the communication link is realized with electric signals transmitted through wired or wireless communication channels. But in principle, the communication link can also be established through mechanical or fluidic connections that allow the transmission of force and displacement between the remote environment and the operator. The goal of the communication link is to allow real-time interaction, which requires a reliable and fast exchange of data between master and slave actuators.[1] The tele-operator presented in this article is a hybrid system that has a communication link in the form of compressed air in pneumatic tubes, where the pressure is controlled using a servo-valve to enhance the passive pneumatic connection.

The need for tele-operators has increased in several domains, especially where geometric and physical constraints might prohibit the direct interaction between the operator and a remote object in order to avoid direct exposure to hazards such as radiation or chemicals, or because the remote location may be unreachable for the human operator such as in deep-sea or space exploration. The system presented in this article is intended for use in a medical context, more specifically for tele-operation under magnetic resonance imaging (MRI) conditions. The system was developed to allow short-distance mechanical two-way interaction between a surgeon in the MRI control room and a patient in the MRI scanner.

Two-way interaction indicates the ability to drive a system from both sides, which requires the slave actuator to be able to reflect the force of the task environment back to the human operator via the master actuator. In this case, the tele-operation system is said to be controlled *bilaterally*.[2] This means that the slave actuator must communicate two physical quantities

[1]American University of Beirut, Beirut, Lebanon
[2]Danfoss Power Solutions GmbH & Co. OHG, Neumünster, Germany

Corresponding author:
Naseem Daher, American University of Beirut, P.O. Box 11-0236, Riad El Solh, Beirut 1107 2020, Lebanon.
Email: nd38@aub.edu.lb

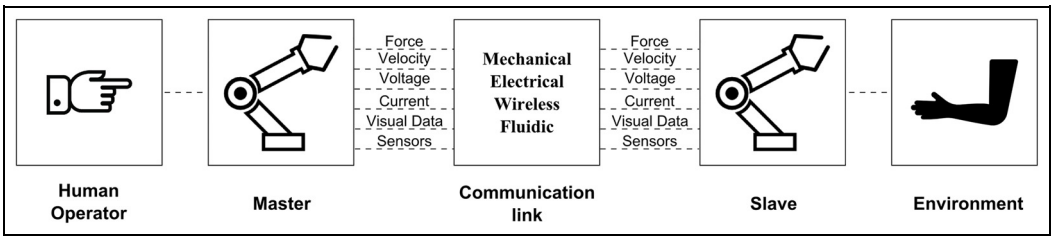

Figure 1. General tele-operation system composition..

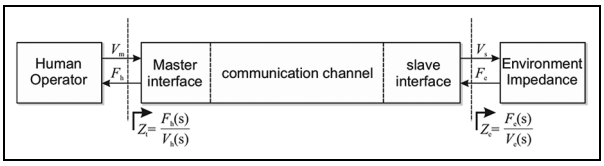

Figure 2. Relationship between tele-operator impedance Z_t and environment impedance Z_e.

back to the master device: force and displacement. If the system is realized based on electrical communication only, both position and force transducers are required. The system presented in this article is a hybrid system with both electrical and fluidic–mechanical communication links and therefore does not prompt the need for a force sensor. Before the new system is presented, the subsequent section briefly discusses the challenge of bilateral control for tele-operation systems by introducing the notions of transparency and stability.

Transparency and stability of tele-operation systems

Bilateral control of tele-operation systems is an active field of research, where the main aim is to improve two critical criteria that qualify the performance of tele-operators: *stability* and *transparency*. It can be shown that stability is increased at the expense of transparency, and vice versa, such that every control design implementation represents a better or worse compromise between these two criteria. Nevertheless, significant improvements have been achieved in the realization of tele-operation systems, where sensory substitution can be used to surrogate a remote resistance without actual force reflection. In Pacchierotti et al.,[3] cutaneous sensation (i.e. stimulation of skin) at the operator hand is used to replace the kinesthetic sensory information (i.e. force feedback) of a remote resistance. whenever kinesthetic feedback needs to be suppressed to increase system stability, a substitutionary skin sensation is produced that can be interpreted by the operator as an increased resistance.

While several factors require the force-feedback gain to be reduced for maintaining stability, latency in the communication link is a critical factor as well. All digitized control systems, especially those that require transmission over long distances, via wired or wireless connection, suffer from latency in the communication link, which is under ongoing research and must be taken into account.[4] As the second enabling factor of tele-operation, transparency is defined as the ratio between the resistance of the master device experienced by the operator and the actual resistance of the remote environment.[5] For a linear time-invariant (LTI) system, resistance (also referred to as impedance) can be expressed in the s-domain as the ratio between the Laplace transform of the resistive force $F(s)$ and the corresponding contact velocity $V(s)$ as

$$Z(s) = \frac{F(s)}{V(s)} \tag{1}$$

Figure 2 shows the various parameters that are communicated between the slave and master actuators, where V_m is the hand velocity of the human operator, F_h is the force reflected by the master actuator, V_s is the slave actuator velocity, and F_e is the force that is reflected by the environment.

Hence, transparency can be simply defined as the ratio between the impedances of the tele-operator, Z_t, and the environment, Z_e

$$\text{Transparency} = \frac{Z_t}{Z_e} \tag{2}$$

where

$$Z_t = \frac{F_h}{V_m} \tag{3}$$

$$Z_e = \frac{F_e}{V_s} \tag{4}$$

The aim of a tele-operator is to equalize the impedance felt by the human operator, Z_t, to the environment impedance, Z_e, which means that the transparency should ideally be unity. However, when considering the frequency response of the transparency function, a value of unity may be achievable for low frequency inputs and starts decreasing at higher frequencies.

However, tele-operation stability is not determined by the tele-operation system alone. As soon as the tele-operation system gets in physical contact with the operator and the environment, their impedance characteristics become part of the system dynamics and have their influence on the overall dynamics.[6] It can be shown that transparency and stability are two competing design goals.[7] Thus, a good tele-operator design strives to accomplish a balanced trade-off between stability and

transparency over a broad range of operating conditions. The quality of the trade-off has to be evaluated in each application with respect to the required performance and alternative solutions.

Pneumatic tele-operators and a brief survey of their control schemes

This section provides a brief overview of several approaches that were adopted to achieve high performing tele-operators, which served as a basis for the proposed design in this work. The first feature of the presented design is the use of pneumatic actuators, given the intended use in MRI environments with short transmission distances. Pneumatic actuators are most suitable for use in MRI environments for a multitude of characteristics: they can be fabricated from non-metallic and non-magnetic materials, they pose minimal risk of leakage hazards, they feature a high force-density ratio, they offer a natural (non-synthetic) compliance that is advantageous for human interaction, they are back-drivable as direct drives, and they are relatively low-cost with accurate precision capabilities.[8,9]

A novel idea of a pneumatic robot that is used for transperineal prostate needle placement for biopsy and brachytherapy seed placement was presented in Fischer et al.[10] The mechanism design fits within the geometrical constraints of the scanner and at the same time guarantees the required motion specified by the operator, which was limited to 2 degrees of freedom: vertical and horizontal. Using sliding-mode control (SMC) to actuate and control the piezo-electrically actuated valves that are situated near the patient, the system was tested and validated under live MRI regarding MR compatibility, workspace, work-flow, localization, and placement accuracies. Another design, implementation, and evaluation of a pneumatically actuated robotic assistant system for real-time MRI-guided aortic valve replacement were presented in Li et al.[11] The system is MRI compatible, with low signal-to-noise ratio of imaging while the robotic arm moves inside the scanner. Using a proportional position loop integral and proportional velocity (PIV) control scheme, the system presented good tracking with minimal position and velocity errors. Another MRI-compatible pneumatic actuator with force feedback was presented in Shang et al.,[12] where the system consisted of a piezo-electrically actuated slave robot that is used for needle placement with an integrated fiber optic force sensor that employs Fabry–Pérot interferometry (FPI) sensing principle. The sensor flexure was integrated in the slave robot to measure the needle insertion force. Combining the complementary features of piezoelectric and pneumatic actuation, a pneumatically actuated haptic master robot was designed to feed the force associated with needle placement interventions back to the clinician. A load cell was utilized to close the impedance feedback control loop of the master robot. A force–position control algorithm was designed to control the hybrid actuated system and yielded accurate tracking performance.

The valve in turn controls the pressures for adaptation to changing operating conditions and environments, where several prior works addressed this key requirement of tele-operation systems. A parameter estimation architecture of the environment was presented in Misra and Okamura,[13] where nonlinear stiffness and damping characteristics of the physical environment were estimated using an indirect adaptive control approach, which yielded improved system transparency. A model-based adaptive controller was designed for the Pneu-WREX robot for rehabilitation in Wolbrecht et al.[14] The controller included a novel Kalman filter realization for state estimation. Flow dynamics of air and leakage were estimated and included in a Lyapunov-based analysis, while experimental data were used to characterize the used servo-valve. An adaptive friction compensation algorithm was proposed in Franco et al.[15] to control a pneumatically actuated master–slave system intended for tele-operated needle insertion in the liver under MRI guidance. The aim was to achieve accurate needle positioning and operator in the presence of friction forces. Experimental results demonstrated improved performance of admittance control over traditional impedance control. An indirect adaptive velocity controller was designed in Daher and Ivantysynova[16] for an electro-hydraulic steer-by-wire system, which uses pump displacement control (DC) actuation to control the motion of a linear single rod steering actuator. A self-tuning regulator was designed and validated, where simulation and experimental results demonstrated the effectiveness of the control system in coping with uncertainties and adapting to varying parameters and loading conditions.

Novel pneumatic tele-operation system

A novelty of the proposed tele-operation system is its 1 degree-of-freedom design with force feedback, and its key feature of a hybrid connection between the master and slave actuators through electric and fluid-mechanical links. The electrical link is used to communicate the difference in position between the slave and master actuators, while the fluid-mechanical link is used to transmit the force information. The position difference is used to control the force communicated between the master and slave actuators. The motivation behind using this hybrid communication link is reducing the number of components as compared to other bilateral tele-operation systems, with the aim of reducing cost and complexity. In particular, no force or pressure sensors are required for the new system, where a pneumatic control valve situated near the master cylinder being the only active component.

A unique feature of the proposed architecture is that the complete tele-operation system is one integrated

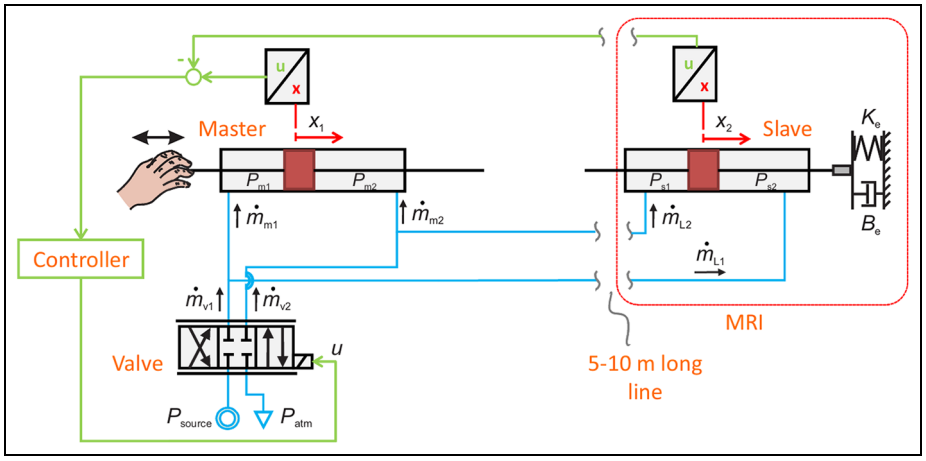

Figure 3. Pneumatic tele-operation system schematic (pneumatic connection in blue).

physical unit (master actuator, pneumatic lines, slave actuator). The connection between the master and slave actuators is not only realized through electrical control but also via physical means. While the conventional bilateral tele-operation architecture[7] assumes two electrical control channels between the master and slave, the presented concept is a combination of one electrical and one fluidic communication channel. In fact, it can be compared to the approaches adopted in Gassert and colleagues,[17,18] where a cable or beam mechanisms are employed. Using beam or cable transmission, both motion and forces can be relayed over short distances. On the other hand, a pneumatic connection has the advantage that the transmission is achieved through a flexible tube, where the compressed air that functions as a transmitting fluid has low density and does not significantly increase the transmission inertia. That said, a disadvantage of a pneumatic architecture is the low stiffness of the fluidic connection.

Figure 3 depicts the components of the proposed system. Master and slave actuators are connected via pneumatic lines (5–10 m long), which establish a physical connection that transmits the force between the operator and the remote environment via pressurized air. Position sensors are connected to each cylinder, and the position difference is fed back to a pneumatic valve that is placed near the master actuator. The valve in turn controls the airflow rates, and consequently, the pressures in the lines connecting the master and slave cylinders. It is essential for the valve to be far away from the slave actuator in order to prevent electromagnetic interfere with the MRI procedure.

The proposed tele-operation system was first presented in Elmasry and Liermann[19] with a cascaded proportional position and pressure feedback control system. The employment of an adaptive control scheme was investigated in Baayoun et al.,[20] which provided a positive outlook on the ability to improve the system transparency over fixed-gain controllers by means of adaptive control. This work includes the assessment of transparency and stability of the proposed tele-operation system and control method, which shows improved results with the design of a simplified second-order indirect self-tuning regulator.

The paper is structured as follows. In the "Dynamic system model" section, the governing equations of the dynamic model are derived. The "Control system design" section presents the proportional and adaptive control designs, followed by a discussion and comparison of the transparency achieved with these designs in the "Transparency assessment" section. Experimental results on the prototype test bench are presented in the "Experimental results" section. The paper concludes with a discussion and outlook provided in the "Conclusion" section.

Dynamic system model

This section introduces the governing equations of the dynamic model. The model architecture is depicted in Figure 4. The environment impedance is indicated on top and the operator impedance is indicated at the bottom. The operator hand force F_h is the input to the master cylinder. It is the result of the force reflected by the hand impedance plus an external force component F_h^* caused by the arm motion that can be introduced as a disturbance.

Pressures, P_{m1} and P_{m2}, in the master cylinder indirectly correspond to the operator's hand force and are communicated to the slave actuator through the pneumatic lines. On the environment side, the force acting on the slave actuator, F_e, is the sum of the reflected force by the environment impedance and an additional external force component, F_e^*, which can be understood as an external disturbance.

The mathematical model can be divided into four main parts that shall be described in the following sections: (a) the actuator motion equation including the environment and operator impedances, (b) the ideal gas and energy conservation laws that relate the cylinder pressures to the piston motion and exchange of air,

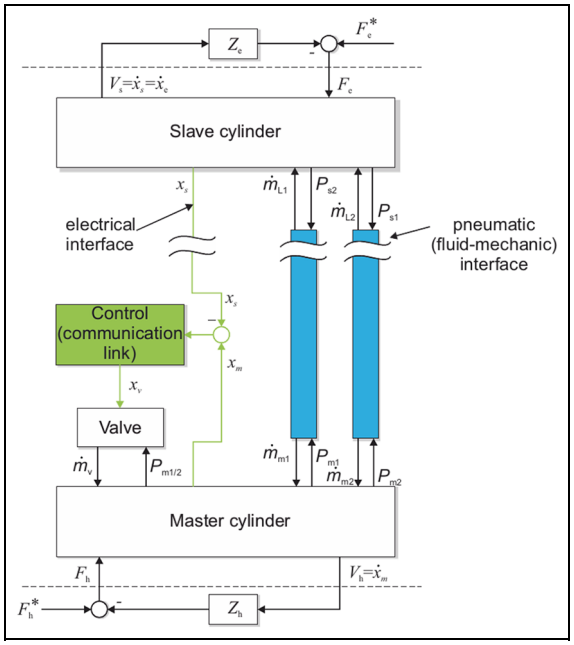

Figure 4. Model architecture of proposed pneumatic tele-operation system. The arrows indicate which variables are inputs and outputs to each sub-model.

(c) the high-response pneumatic valve, and (d) the long tube dynamics. These four parts and the interfacing variables are visualized in Figure 4.

Actuator motion

The force transmitted to the human operator, assuming zero coulomb friction given the ultra-low friction characteristic of the utilized actuators, is given by

$$F_h = (P_{m1} - P_{m2})A_p - m_p\ddot{x}_m - \beta\dot{x}_m \tag{5}$$

where A_p is piston's cross-sectional area, x_m is the position of the master piston, m_p is the mass of the piston, and β is the viscous friction coefficient of the pistons. Coulomb friction is neglected due to the ultra-low friction cylinders, which are used in this application, and considering that the dynamic model is primarily intended for model-based control system design. All plant parameter values, as obtained from measurement, can be found in Table 1. The equation of motion of the slave piston is given by

$$m_p\ddot{x}_s + \beta\dot{x}_s = (P_{s1} - P_{s2})A_p - B_e\dot{x}_s - K_e x_s \tag{6}$$

where x_s is the position of the slave piston, B_e is the damping coefficient, and K_e is the equivalent spring constant of the environment impedance model.

Cylinder chamber pressure drop

Since rapid movement is not expected in this specific tele-operation application, isothermal compression is assumed for modeling the cylinder pressures. Master

Table 1. Nomenclature..

Symbol	Comment	Value	Unit
A_p	Piston area	420.7201	mm^2
A_l	Cross-sectional area of the pneumatic line	12.5664	mm^2
b	Critical pressure ratio given by the valve manufacturer	0.21	
c	Sonic conductance of valve	0.45	L/bar s
D	Tube inner diameter	4	mm
D_p	Piston diameter	11.57	mm
F_h	Hand force		N
K_v	Electromechanical valve gain	0.2	1/V
L	Pneumatic line length	10	m
l_{cyl}	Total cylinder stroke	275	mm
$\dot{m}_{1m}$	Mass flow rate into chamber 1 of master		kg/s
m_p	Mass of the piston	0.2546	kg
$P_{m/s,\,1/2}$	Master/slave pressure in chamber 1 or 2		Pa
$P_{u/d}$	Upstream/downstream pressure of valve		Pa
P_s	Pressure supply to the valves	3	bar
P_{atm}	Atmospheric pressure	1	bar
R	Ideal gas constant	2.87	bar L/kg K
T_0	Temperature of air at reference conditions		K°
T_1	Upstream temperature of valve		K°
u	Valve input signal		V
V_{m1}	Volume of chamber 1 of master		m^3
V_{md}	Dead volume of master	0.002	m^3
$\bar{w}$	Mean air velocity through the pneumatic line		m/s^2
x_h	Hand position		m
$x_{m/s}$	Master/slave piston position		m
x_v	Relative spool opening of valve		m
β	Viscous friction of the cylinders	0.0116	N s/mm
μ	Dynamic viscosity of air	1.8127×10^{-8}	kg/mm s
ν	Air kinematic viscosity	1.568×10^{-5}	m^2/s
ρ_0	Density of air at reference conditions	0.0012	kg/L

and slave cylinders are governed by the same set of equations; we suffice to present the equations for the master cylinder. By applying the ideal gas and energy conservation laws, the rate of change of the pressure in chamber 1 of the master cylinder can be written as

$$\dot{P}_{m1} = \frac{RT}{V_{m1}}\dot{m}_{m1} - \frac{P_{m1}}{V_{m1}}\dot{V}_{m1} \tag{7}$$

where P_{m1} is the pressure in chamber 1, V_{m1} is the volume of chamber 1, R is the ideal gas constant, T is the chamber temperature, and $\dot{m}_{m1}$ is the entering mass flow rate. The latter is the difference of mass flow rate coming from the valve and exiting into the tube

$$\dot{m}_{m1} = \dot{m}_{v1} - \dot{m}_{L1} \tag{8}$$

The volume of chamber 1 of the master cylinder can be expressed in terms of piston position as

$$V_{m1} = V_{md} + x_m A_p \tag{9}$$

where V_{md} is the dead volume of the chamber and x_m is the piston position of the master cylinder. Substituting equation (9) into equation (7) yields

$$\dot{P}_{m1} = \frac{RT}{V_{md} + x_m A_p}\dot{m}_{m1} - \frac{P_{m1}}{V_{md} + x_m A_p}\dot{x}_m A_p \tag{10}$$

The pressure gradient equation for chamber 1 of the slave actuator is obtained by replacing subscript m by s. Similarly, the pressure gradient in chamber 2 is expressed as

$$\dot{P}_{m2} = \frac{RT}{V_{md} + (l_{cyl} - x_m)A_p}\dot{m}_{m2} + \frac{P_{m2}}{V_{md} + (l_{cyl} - x_m)A_p}\dot{x}_m A_p \tag{11}$$

Valve flow equation

As shown in Figure 5, the valve connects the transmission tubes either to the pressure supply or to the atmosphere based on its spool position, x_v, which is controlled by the input u.

The mass influx of the valve, $\dot{m}_{vn}$, depends on the control input, u, and the downstream and upstream pressures. It is commonly expressed as[21]

$$\dot{m}_v = \begin{cases} u c \rho_0 P_u \sqrt{\frac{T_0}{T_1}} \sqrt{1 - \left(\frac{\frac{P_d}{P_u} - b}{1 - b}\right)^2} & \text{for } \frac{P_d}{P_u} > b \\ u c \rho_0 P_u \sqrt{\frac{T_0}{T_1}} & \text{for } \frac{P_d}{P_u} \leqslant b \end{cases} \tag{12}$$

where c is the sonic conductance, ρ_0 is the air density at reference conditions, P_u is the upstream pressure, P_d is the downstream pressure, T_0 is the air temperature at reference conditions, T_1 is the upstream air temperature, and b is the critical pressure ratio as specified by the servo-valve manufacturer. The natural frequency of the servo-valve spool position control is 125 Hz and can therefore be neglected given its relatively fast dynamics.

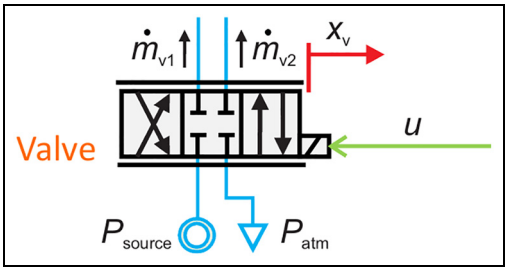

Figure 5. Pneumatic control valve schematic.

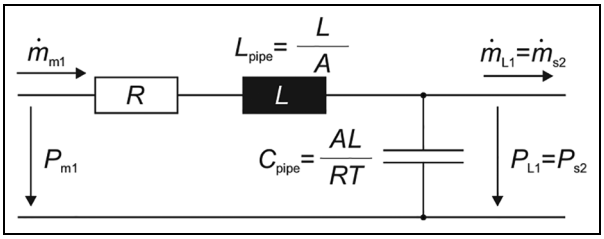

Figure 6. Tube model.

Tube modeling

Isothermal compression is assumed for the tube dynamics. This is considered a valid assumption if the largest frequency f (rad/s) meets the condition[22]

$$f \leqslant \frac{4\nu}{A} \tag{13}$$

where ν is the kinematic viscosity and A the tube's cross-sectional area. The tubes can be modeled with one or more elements using simple resistance, capacitance, and inertance characteristics,[23] as shown in Figure 6. In this work, only one element is considered.

The capacitance is the result of compressibility of the air in the fixed volume of the tube. For isothermal conditions, the ideal gas law and energy conservation law give the equation for the gradient of pressure, similar to equation (10) as

$$\dot{P}_{L1} = \frac{RT}{AL}(\dot{m}_{L1} - \dot{m}_{s2}) \tag{14}$$

However, since we can see from Figure 6, that the capacitance of the tube is directly connected with the slave cylinder chamber with

$$P_{L1} = P_{s2} \tag{15}$$

it follows that the volume of the tube from a modeling point of view is simply added to the volume of the slave cylinder chamber.

The large length of the tube compared to its cross section results in a significant inertance. The acceleration of air is caused by the pressure difference across the tube and lessened by friction

$$\frac{d\dot{m}_{L1}}{dt} = \frac{A}{L}(P_{m1} - P_{L1} - \Delta p_{friction}) \tag{16}$$

where the pressure drop caused by laminar friction is given by

$$\Delta P_{friction} = \frac{32\mu\bar{w}L}{D^2} = \frac{32\mu\dot{m}_{L1}L}{\rho A D^2} \tag{17}$$

Model reduction

The derived nonlinear model equations can be linearized resulting in a seventh-order linear model without loss of fidelity.[20] It can be expressed as a linearized state-space system where the state vector, X, is given by $X = [x_s; \dot{x}_s; P_s; \dot{m}; x_m; \dot{x}_m; P_m]$. The state equations are

$$\dot{x}_s = \dot{x}_s \tag{18}$$

$$\ddot{x}_s = -\frac{1000k_e}{m_p + m_e}x_s - \frac{1000(\beta + B_e)}{m_p + m_e}\dot{x}_s - \frac{1000 \cdot 0.1A_p}{m_p + m_e}P_s \tag{19}$$

$$\dot{P}_s = (c_6 + c_8)\dot{x}_s + (c_7 + c_5)\dot{m} \tag{20}$$

$$\ddot{m} = -c_{11}P_s - c_{13}\dot{m} + c_{11}P_m \tag{21}$$

$$\dot{x}_m = \dot{x}_m \tag{22}$$

$$\ddot{x}_m = -\frac{1000k_h}{m_p + m_h}x_m - \frac{1000\beta}{m_p + m_h}\dot{x}_m + \frac{1000 \cdot 0.1A_p}{m_p + m_h}P_m + \frac{1000}{m_p + m_h}F_h \tag{23}$$

$$\dot{P}_m = \frac{-c_{12}}{(c_1 + c_{12})(c_1 + c_3)}\dot{m} - \frac{c_{12}}{(c_1 + c_{12})(c_2 + c_4)}\dot{x}_m - \frac{K_v c_{12}}{(c_1 + c_{12})(c_1 c_9 + c_3 c_{10})}P_m + \frac{K_v c_{12}}{(c_1 + c_{12})(c_1 c_9 + c_3 c_{10})}u \tag{24}$$

where $c_{1\ldots13}$ are constants defined in Appendix 1.

The output equation is the position difference between the master and slave

$$y = x_m - x_s \tag{25}$$

The reduced seventh-order system is dependent on the contact environment as illustrated in Figure 7, which shows the frequency response of the open-loop system with the valve position as input, and the position difference between master and slave actuators $(x_m(t) - x_s(t))$ as output. The environment is modeled as a spring with varying stiffness of $0 - 10\,\mathrm{N/mm}$ in increments of $2.5\,\mathrm{N/mm}$.

It is noted that higher order dynamics are more prevalent at frequencies exceeding 3 Hz. Sensitivity analysis also shows that the frequency response of the open-loop system varies as other parameters, such as the mass and damping coefficient of the contact environment, are varied. Since the main intent of the modeling effort centers around deriving a model that lends itself well to control system design, the dynamic model is further reduced to only capture the frequency range of typical operating conditions of the proposed tele-operation system of less than 20 rad/s. The system is thus reduced to second order, whose transfer function accurately represents the higher order system in the frequency domain of interest, as shown in Figure 8, which paves the way in front of designing a reduced order self-tuning regulator.

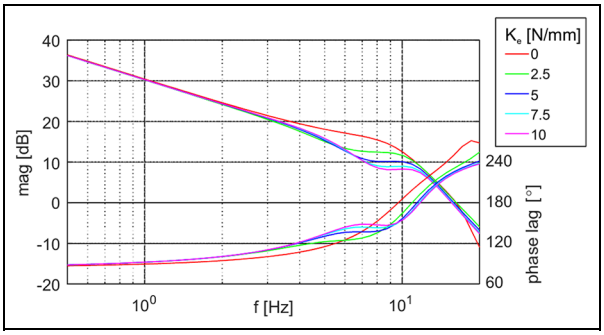

Figure 7. Open-loop frequency response comparison (varying environments).

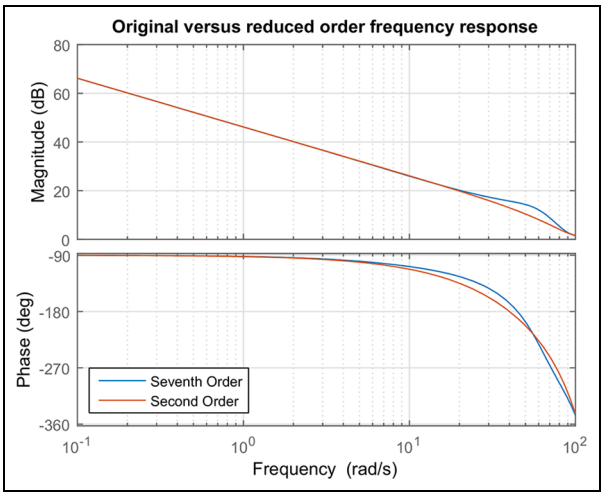

Figure 8. Open-loop frequency response comparison (original vs reduced).

Control system design

Two control system design schemes are presented in this section: a cascaded fixed-gain proportional controller and an adaptive controller in the form of an indirect self-tuning regulator.

Fixed-gain controller

A fixed-gain proportional position feedback control with cascaded pressure feedback was applied to the tele-operation system in Elmasry and Liermann[19] (Figure 9). The control parameters that ensured accurate tracking of the master and slave actuators with guaranteed stability were found to be $K_p = 2.9\,\mathrm{V/bar}$ and $K_s = 2.4\,\mathrm{N/mm}$. The adaptive controller that is

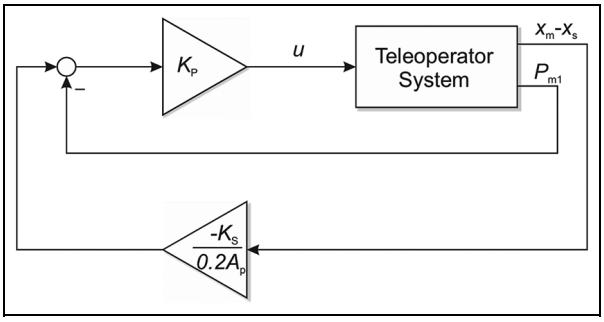

Figure 9. Fixed-gain proportional control system.[19].

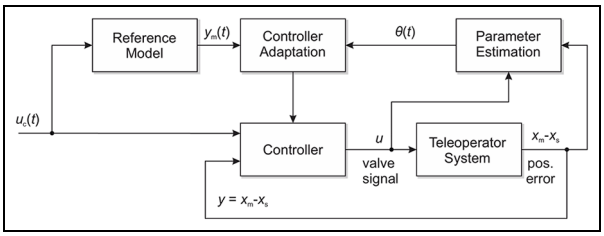

Figure 10. Block diagram of the adaptive control system.

developed in this work will be compared to this proportional controller, which serves as a baseline for benchmarking purposes.

Adaptive control design

The structure of the adaptive control system revolves around the objective of having the slave actuator track a reference position that is provided by the master actuator, with the aim of minimizing the position tracking error, $x_m - x_s$. Since the system dynamics include the operator and environment impedances, which can significantly vary based on the operating conditions, the model equations are subject to considerable parameter changes. An indirect self-tuning regulator is adopted given its ability to cope with parametric uncertainty to achieve a desired response with asymptotic output tracking, its relatively simple design process, and its low computational expense.

The block diagram of the adaptive controller is given in Figure 10, which shows the tele-operator system having only one input being the valve position, and one output being the position error. The controller receives the reference signal, u_c, and the tele-operator position error as an input. The adaptive controller is designed so that the system output, $y = x_m(t) - x_s(t)$, tracks the reference input, $u_c(t)$, which is a desired zero reference. The control parameters are varied based on the controller adaptation dynamics, which involve the reference model specification and the estimated plant parameters. The indirect self-tuning regulator is designed without zero cancelation to minimize oscillations in the control signal, since the plant zero is not well damped.[24] A recursive least squares algorithm is used to estimate the plant parameters. The estimation scheme estimates the system parameters based on the system output and its input, which is the servo-valve control signal, $u(t)$. The following two sections outline the design process of the online estimator and the adaptive controller.

Parameter estimation. In discretized form, the reduced second-order system model has the following plant transfer function

$$G(z) = \frac{B(z)}{A(z)} = \frac{b_0 z + b_1}{z^2 + a_1 z + a_2} = \frac{y}{u} \tag{26}$$

Dividing by z^2 yields

$$A(z^{-1})y(t) = B(z^{-1})u(t) \tag{27}$$

$$(1 + a_1 z^{-1} + a_2 z^{-2})y(t) = (b_0 z^{-1} + b_1 z^{-2})u(t) \tag{28}$$

The system is expressed as a difference equation as

$$y(t) = -a_1 y(t-1) - a_2 y(t-2) + \cdots + b_0 u(t-1) + b_1 u(t-2) \tag{29}$$

The parameter vector, $\theta(t)$, and the regression vector, $\varphi^T(t)$, are given by

$$\theta(t) = [a_1, a_2, b_0, b_1]^T \tag{30}$$

$$\varphi^T(t) = [-y(t-1), -y(t-2), u(t-1), u(t-2)] \tag{31}$$

The output $y(t)$ is then expressed as

$$y(t) = \varphi^T(t)\theta \tag{32}$$

A recursive least square estimation scheme is given by

$$\hat{\theta}(t) = \hat{\theta}(t-1) + K(t)[y(t) - \varphi^T(t)\hat{\theta}(t-1)] \tag{33}$$

$$K(t) = P(t-1)\varphi(t)[I + \varphi^T(t)P(t-1)\varphi(t)]^{-1}$$
$$P(t) = [I - K(t)\varphi^T(t)]P(t-1) \tag{34}$$

where $P(t) = (\varphi^T(t)\varphi(t))^{-1}$. Vector $K(t)$ consists of the weighting factors that determine how the correction and previous estimates are combined. Parameter vector $\theta(t)$ is initialized with values that are expected from nominal modeling of the system, and the $P(t)$ matrix is initialized with a 4×4 identity matrix multiplied by a sufficiently large number to achieve asymptotic output tracking. Since the system parameters do not rapidly change, parameter estimation is not performed at each sampling time of the controller, which is computationally more efficient. The sampling time of the parameter estimation is chosen as 30 ms, while the controller sampling time is 1 ms.

Controller design. A control law that yields 2 degrees of freedom, feed-forward and negative feedback, is given by

$$Ru(t) = Tu_c(t) - Sy(t) \tag{35}$$

where R, T, and S are polynomials determined by the controller design based on the estimated plant parameters and the specified reference model. A standard continuous-time transfer function of a second-order reference model is given by

$$\frac{B_m(s)}{A_m(s)} = \frac{\omega_n^2}{s^2 + 2\zeta\omega_n s + \omega_n^2} \tag{36}$$

where ω_n is the undamped natural frequency and ζ is the damping ratio. The desired dynamic response is defined by setting the undamped natural frequency and the damping ratio to specified values that achieve the desired tracking performance and transient response. In this work, based on desired performance specifications of the tele-operation system, $\omega_n = 132\,\text{rad/s}$ and $\zeta = 1$ to obtain a 10%–90% rise time of 0.025 s and a critically damped transient response with no overshoot, which is desired in surgical procedures. With a sampling time of 1 ms, the discretized transfer function of the reference model is given by

$$\begin{aligned}\frac{B_m(z)}{A_m(z)} &= \frac{b_{m0}z + b_{m1}}{z^2 + a_{m1}z + a_{m2}} \\ &= \frac{0.007976z + 0.007304}{z^2 - 1.753z + 0.7681}\end{aligned} \tag{37}$$

Since the indirect self-tuning regulator is designed without zero cancelation, given that the plant zero is not well damped, polynomial $B(z)$ can be written as

$$B(z) = B^+(z)B^-(z)$$
$$B^+(z) = 1$$
$$B^-(z) = B(z)$$

The causality conditions that specify the relative degrees of the observer polynomial, A_O, and polynomials R, S, and T are

$$degA_O = degA - degB^+ - 1 = 1$$
$$degR = deg(A_O A_m) - degA$$
$$degS \leqslant degR$$
$$degT \leqslant degR$$

The control signal, $u(t)$, is obtained from equation (35) as

$$u(t) = \frac{T}{R}u_c(t) - \frac{S}{R}y(t) \tag{38}$$

Elimination of $u(t)$ given by equation (26) yields the system output, $y(t)$, as a function of the commanded input, $u_c(t)$

$$y(t) = \frac{BT}{AR + BS}u_c(t) \tag{39}$$

Without adaptation, the system has the format of a state controller with an observer design, and it can be shown that the transfer function becomes

$$\frac{y(t)}{u_c(t)} = \frac{BT}{A_O A_m} \tag{40}$$

where A_m is the polynomial that sets the desired pole locations of the reference model, and A_O is the observer polynomial. Polynomial B in equation (26) contains the plant zeros, but since the plant parameters can always vary based on the operating environment, it is only available as an estimate. The observer polynomial $A_O(z)$ is a first-order polynomial, and in discrete form, it is expressed as

$$A_O(z) = z + a_{O1} \tag{41}$$

In discrete-time analysis, using smaller values for the observer poles leads to faster parameter estimation convergence rates[25]; thus, in this work, it is set to zero ($a_{O1} = 0$).

Combining equations (39) and (40) yields

$$AR + BS = A_O A_m \tag{42}$$

which is known as the Diophantine equation.[26] Polynomials A_O and A_m are given via performance specifications, polynomials A and B are provided by the online estimator; thus, polynomials R and S can be computed. Based on the causality conditions, R, S, and T are first-order polynomials

$$R(z) = r_0 z + r_1 \tag{43}$$
$$S(z) = s_0 z + s_1 \tag{44}$$

The control design objective is for the closed-loop dynamics (equation (39)) to follow the reference model dynamics (equation (36)). It follows from equation (40) that the feed-forward term, T, is

$$T = \frac{B_m}{B}A_O \tag{45}$$

which can be computed as

$$T = \left.\frac{A_m}{B}\right|_{z=1} A_O \tag{46}$$

In discrete form, $T(z)$ is written as

$$T(z) = t_0 z + t_1 \tag{47}$$

The control signal $u(t)$ is saturated between –1 and 1 corresponding to the minimum and maximum normalized servo-valve spool positions, where a maximum value of $u(t) = 1$ corresponds to the full opening of the valve.

Transparency assessment

Transparency is formally defined in equation (2) for linear systems. For certain operating conditions, an assessment of the transparency can be made by comparing the impedance of the tele-operator Z_t, which is the impedance transmitted to the human operator, to the impedance of the environment Z_e as shown in Figure 2.

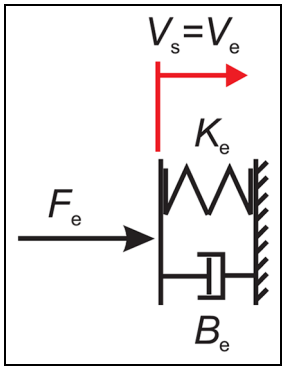

Figure 11. Environment representation.

If the environment is modeled as a spring–damper system, as shown in Figure 11, its impedance is given by

$$Z_e = \frac{B_e s + K_e}{s} \tag{48}$$

As previously mentioned, the transparency ratio should ideally be unity, that is, the impedance transmitted to the operator should perfectly match that of the environment. Figure 2 and equation (2) illustrate that the transparency ratio depends on the environment impedance; thus, it is expected to achieve adequate transparency for soft environments with small values of Z_e as compared to stiffer environments. In this study, the transparency analysis is performed for a relatively soft environment with a spring stiffness of $K_e = 0.4\,\mathrm{N/mm}$ and zero damping. For the adaptive control system, the tele-operator impedance Z_t is computed via equation (3) and it is characterized by the magnitude ratio and phase shift of the master versus slave pistons via simulation for eight frequencies: $0.1, 0.4, 0.5, 1, \pi, 5$, and $10\,\mathrm{rad/s}$. The resultant transparency is plotted on a Bode diagram in Figure 12.

For the proportional controller, the transparency ratio at low frequencies is $-5.2\,\mathrm{dB}$ corresponding to a factor 0.55, which implies that the system feels to the operator about half as stiff as the environment. On the other hand, it is seen that for the adaptive controller, the magnitude of the transparency ratio is closer to the $0\,\mathrm{dB}$ line, and that the phase angle is also closer to 0°. This demonstrates a significant improvement of the adaptive controller over its proportional counterpart, especially in the critical low frequencies range. This allows the operator to get a better impression of the remote environment, as the slave actuator closely follows the master actuator with smaller position error and reduced phase lag.

The reduction in the phase shift that is achieved in the transparency of the adaptive system is indeed significant. The difference in phase angle between the tele-operator impedance and the environment impedance leads to a non-zero phase of transparency. A positive value of the phase angle corresponds to the impression of the operator that the remote environment does not merely behave like a spring, but also has damping characteristics. Hence, the adaptive controller succeeds at reducing the effect of a synthetic feel of additional damping as compared to the proportional controller. What is observed in the frequency domain is also reflected in the time domain. Figure 13 shows the sinusoidal responses of the proportional and adaptive controllers by plotting the positions of both cylinders, during which a force of 10 N is applied at a frequency of $\pi\,\mathrm{rad/s}$ to the master actuator. An improved transparency can be clearly seen in the case of the adaptive control system, given the smaller tracking error between the master and slave actuators, and the reduced phase shift between the actuator positions. In both cases, the slave actuator travels approximately the same distance against the spring environment. However, in the adaptive controller case, the system behaves stiffer and the master actuator tracks the motion of the slave actuator with small tracking error. On the other hand, the proportional controller results in larger tracking errors and phase shift than the adaptive controller.

Test setup

The experimental setup of the tele-operation system comprises off-the-shelf pneumatic components, albeit without an initial effort to make the system MRI compatible. MRI safety requires the use of non-magnetic and non-conductive materials for the master actuator and its position measurement system. In a practical application, an optical encoder can be used as a position sensor and a pneumatic cylinder can be built entirely from non-magnetic material. The experimental setup is depicted in Figure 14.

The cylinders are ultra-low friction double-rod cylinders (Airpel M-24-D-275.0-D-T1T4) having a stroke of 275 mm, a bore diameter of 24 mm, and a rod diameter of 6.35 mm. Their low friction characteristic is achieved by a graphite piston sliding in a precision glass tube. They are cross-connected as shown in Figure 3 by two polyurethane pneumatic tubes of 4 mm inner diameter. A five-port/three-way high-response proportional servovalve (Festo MPYE-5-M5-010-B) connects the two pneumatic tubes near the master cylinder ports with the supply pressure and atmospheric exhaust. The valve is characterized by a bandwidth of 125 Hz, a sonic conductance, $c = 0.45\,\mathrm{L/bar\,s}$, and a critical pressure ratio, $b = 0.21$. The air supply is filtered by a 5-μm mesh and an additional coalescent filter. The rod of each cylinder is connected to a resistive position sensor (Festo MLE-POT-500-TLF and OPKON ELPT) and the pressures in each line are monitored near the master cylinder ports (Festo SPTW-P2R-G14-A-M12). The control system is implemented on a Linux operating system using the open-source RealTime Application Interface (RTAI) for Linux. The Linux RTAI kernel modification facilitates the implantation of the control program as a

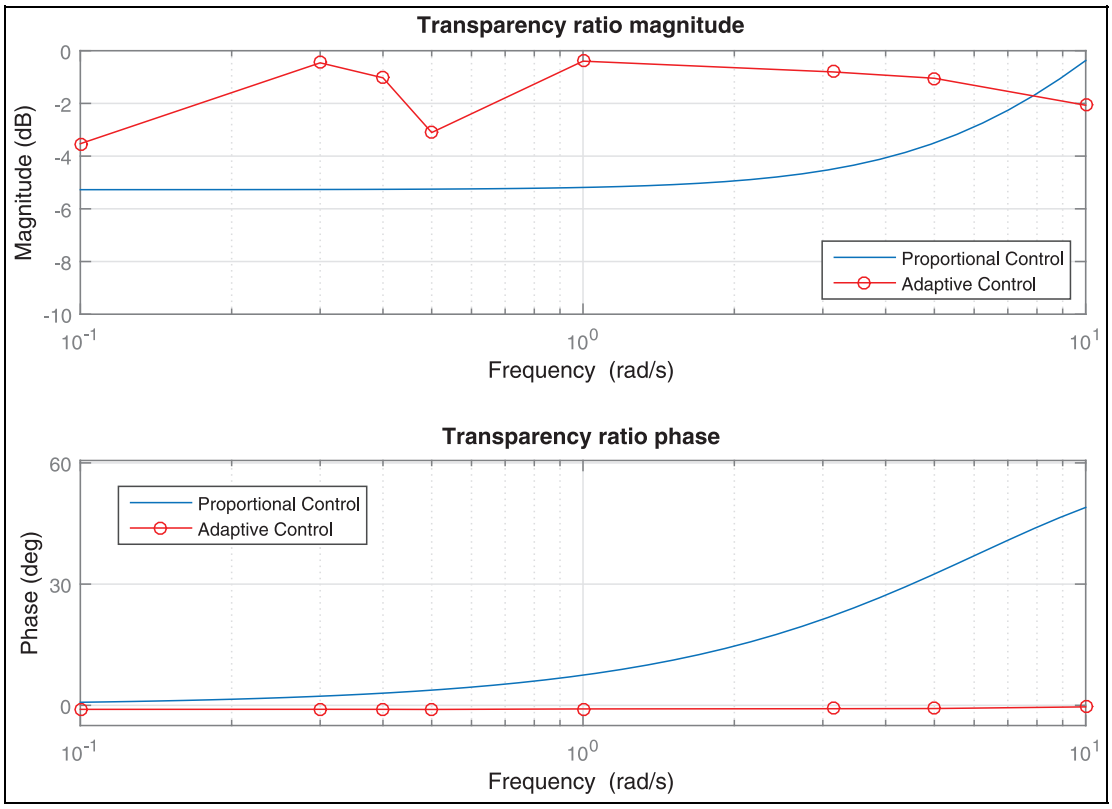

Figure 12. Transparency ratio comparison of the adaptive and proportional controllers against a spring.

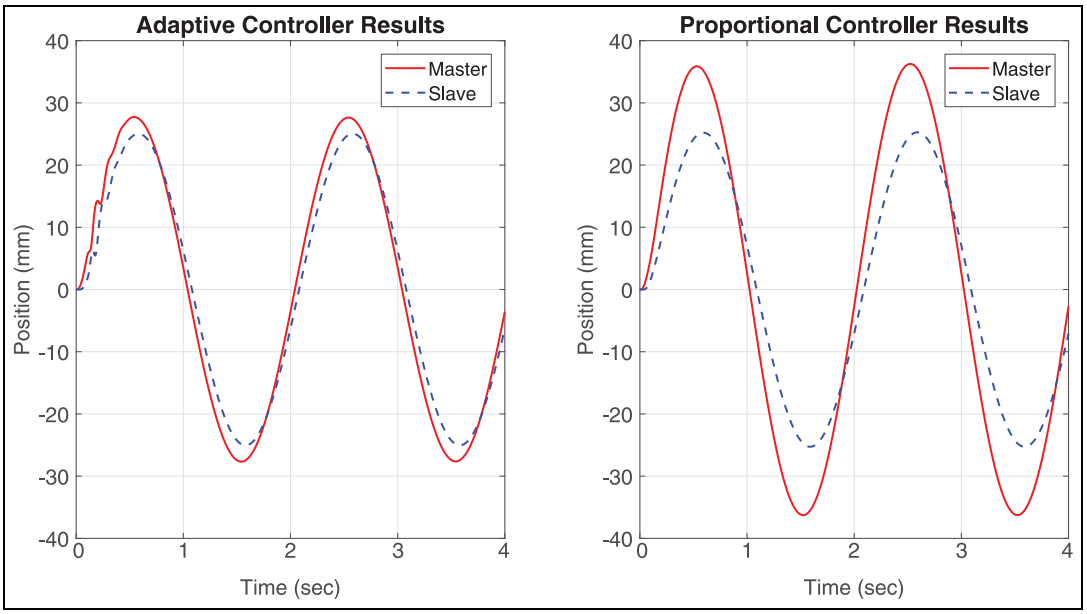

Figure 13. Adaptive (left) and proportional (right) controller simulation results when the slave actuator acts upon a spring.

module in the kernel (as opposed to the application layer) and guarantees highest execution priority at specified time intervals. The control program is generated with Etherlab, an open-source software suite developed and maintained by Ingenieurgemeinschaft IgH. Etherlab makes use of the MATLAB/Simulink Coder toolbox to produce a control program from a Simulink model. It also provides component libraries for several industrial EtherCat I/O terminals that can be conveniently used to establish the interfacing between the Simulink program and the I/O hardware. The I/O terminals used in this setup are analog differential inputs (Beckhoff EL3104) and analog differential outputs (Beckhoff EL4134). The terminals communicate with

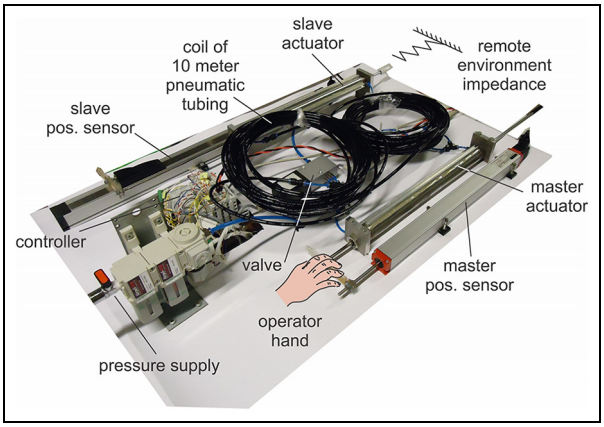

Figure 14. The test rig used in experiment, showing its different components.

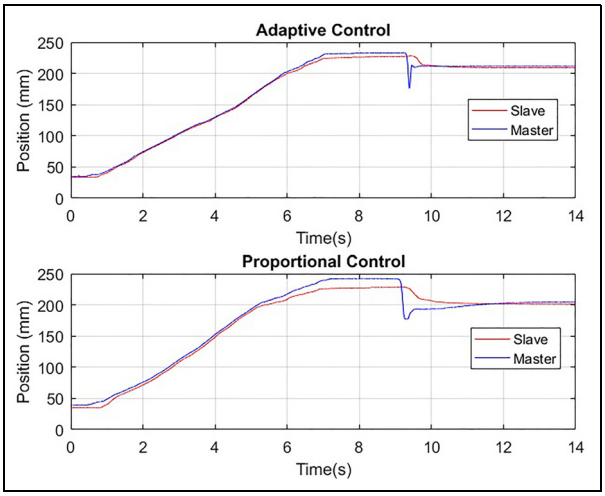

Figure 15. Proportional and adaptive controller results when the slave actuator is facing a spring.

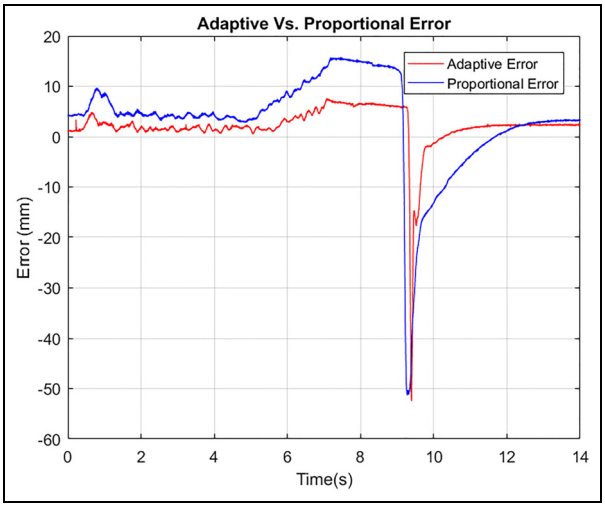

Figure 16. Position error for both adaptive and proportional controllers.

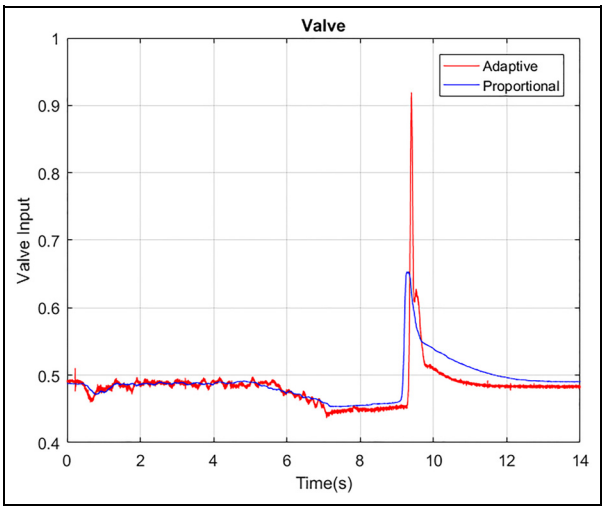

Figure 17. Servo-valve input signal for the adaptive and proportional controllers.

the control program through high-speed serial data communication protocol EtherCat.

Experimental results

The "Transparency assessment" section presents a quantitative comparison of the transparency between the proportional and adaptive control based on numerical simulations. For proper assessment, it is necessary to have a controlled sinusoidal force input, and to measure the reflected force at the interface to the environment. Due to the absence of a load simulator in this work, quantitative transparency assessment can be carried out in simulation only. However, the measurement results obtained from the experimental setup confirm the simulation findings, thus allowing for further discussion and interpretation. The experiment is conducted in the following manner:

- The operator first applies a constant force forward on the master actuator while the slave actuator is free to move (no environment) for around 5 s.
- The slave actuator contacts the spring and compresses it for about 35 mm.
- The operator holds the compressed position for around 1 s.
- The operator suddenly removes the hand force from the master actuator.

The last step is performed in order to check the system performance and stability due to a sudden change in the operator's input. Figure 15 shows the positions of the master and slave actuators under adaptive (top) and proportional (bottom) control. Figure 16 presents the position error between the master and slave actuators for the two controllers, and Figure 17 shows the

servo-valve input signal for the adaptive and proportional controllers.

The experimental results confirm that the adaptive control system has several advantages over its proportional counterpart. In particular, it is able to achieve a smaller position error during free motion as well as during penetration into a spring-based medium; furthermore, following a sudden release of the hand force, it requires less than 1 s to drive the error back to near zero, while the proportional controller requires around 3 s for the position of the slave actuator to match that of the master actuator. It is noteworthy to mention that the difference seen in the graphs is also felt, subjectively, by the operator.

Conclusion

An adaptive controller is designed to control a novel pneumatic tele-operator system, which offers reduced complexity and works in a bilateral mode without the use of a force sensor given the hybrid communication link (pneumatic transmission and electric control of the pressure) between the master and slave actuators. Given that the tele-operator system dynamics change when in contact with various environments, the proposed adaptive controller allows it to cope with these changes. The designed controller is validated under different operating conditions against a baseline proportional controller, both in simulation and experimentally, on a prototype test rig. The adaptive controller offers improved transparency, larger bandwidth, increased stiffness, and improved robustness as compared to the proportional controller. Experimental results show that the adaptive controller yields smaller position tracking error when in contact with different physical environments as compared to the proportional controller. In addition, adaptation occurs in a prompt fashion, even when sudden actions are introduced on both sides of the tele-operator. In conclusion, designing an adaptive controller leads to improved tele-operator performance with the ability to adapt to changes in system parameters. Based on the obtained results, the proposed indirect self-regulating regulator is a suitable choice for this type of tele-operation systems. Future work entails the design and implementation of a Lyapunov-based model reference adaptive control (MRAC) design for comparison with the proposed self-tuning regulator, as it provides a rigorous mathematical proof of stability. Furthermore, the implementation of the proposed architecture in MRI environments will be completed under the guidance of skilled surgeons, in order to validate its performance in real-life situations toward its adoption in surgical procedures.

Declaration of conflicting interests

The author(s) declared no potential conflicts of interest with respect to the research, authorship, and/or publication of this article.

Funding

The author(s) disclosed receipt of the following financial support for the research, authorship, and/or publication of this article: This study was funded by the University Research Board (URB) at the American University of Beirut (AUB).

ORCID iD

Naseem Daher https://orcid.org/0000-0002-3292-0261

References

1. Sheridan T. Telerobotics. *Automatica* 1989; 25(4): 487–507.
2. Hokayem PF and Spong MW. Bilateral teleoperation: an historical survey. *Automatica* 2006; 42(12): 2035–2057.
3. Pacchierotti C, Tirmizi A, Bianchini G, et al. Improving transparency in passive teleoperation by combining cutaneous and kinesthetic force feedback. In: *Proceedings of the 2013 IEEE/RSJ international conference on intelligent robots and systems*, Tokyo, Japan, 3–7 November 2013, pp.4958–4963. New York: IEEE.
4. Jazayeri A and Tavakoli M. Absolute stability analysis of sampled-data scaled bilateral teleoperation systems. *Control Eng Pract* 2013; 21: 1053–1064.
5. Zhu M and Salcudean SE. Achieving transparency for teleoperator system under position and rate control. In: *Proceedings of the 1995 IEEE/RSJ international conference on intelligent robots and systems. Human robot interaction and cooperative robots*, Pittsburgh, PA, 5–9 August 1995, pp.7–12. New York: IEEE.
6. Jazayeri A and Tavakoli M. Revisiting Llewellyn's absolute stability criterion for bilateral teleoperation systems under non-passive operator or environment. In: *Proceedings of the 2012 IEEE/RSJ international conference on intelligent robots and systems*, Vilamoura, 7–12 October 2012, pp.70–75. New York: IEEE.
7. Lawrence D. Stability and transparency in bilateral teleoperation. *Robot Automat IEEE Trans* 1993; 9(5): 624–637.
8. Yu N, Hollnagel C, Blickenstorfer A, et al. Comparison of MRI-compatible mechatronic systems with hydrodynamic and pneumatic actuation. *IEEE/ASME Trans Mech* 2008; 13(3): 268–277.
9. Comber D and Barth EJ. Precision position tracking of MR-compatible pneumatic piston-cylinder using sliding mode control. In: *Proceedings of the ASME 2011 dynamic systems and control conference*, Arlington, VA, 31 October–2 November 2011, pp.45–51. New York: ASME.
10. Fischer GS, Iordachita I, Csoma C, et al. MRI-compatible pneumatic robot for transperineal prostate needle placement. *IEEE/ASME Trans Mech* 2008; 13(3): 295–305.
11. Li M, Kapoor A, Mazilu D, et al. Pneumatic actuated robotic assistant system for aortic valve replacement under MRI guidance. *IEEE Trans Biomed Eng* 2001; 58(2): 443–451.
12. Shang W, Su H, Li G, et al. Teleoperation system with hybrid pneumatic-piezoelectric actuation for MRI-guided needle insertion with haptic feedback. In: *Proceedings of the 2013 IEEE/RSJ international conference on intelligent*

robots and systems (IROS), Tokyo, Japan, 3–7 November 2013, pp.4092–4098. New York: IEEE.
13. Misra S and Okamura A. Environment parameter estimation during bilateral telemanipulation. In: *Proceedings of the 14th symposium on haptic interfaces for virtual environment and teleoperator systems*, Alexandria, VA, 25–26 March 2013, pp.301–307. New York: IEEE.
14. Wolbrecht ET, Reinkensmeyer DJ and Bobrow JE. Pneumatic control of robots for rehabilitation. *Int J Robot Res* 2009; 29: 23–38.
15. Franco E, Rea M, Gedroyc W, et al. Control of a master-slave pneumatic system for teleoperated needle insertion in MRI. *IEEE/ASME Trans Mech* 2016; 21(5): 2595–2600.
16. Daher N and Ivantysynova M. An indirect adaptive velocity controller for a novel steer-by-wire system. *J Dyn Syst Meas Control* 2014; 136(5): 051012.
17. Gassert R, Yamamoto A, Chapuis D, et al. Actuation methods for applications in MR environments. *Concepts Mag Reson Pt B* 2006; 29B(4): 191–209.
18. Chapuis D, Gassert R, Ganesh G, et al. Investigation of a cable transmission for the actuation of MR compatible haptic interfaces. In: *The first IEEE/RAS-EMBS international conference on biomedical robotics and biomechatronics, 2006*, Pisa, 20–22 February 2006, pp.426–431. New York: IEEE.
19. Elmasry A and Liermann M. Passive pneumatic teleoperation system. In: *Proceedings of the ASME/BATH 2013 symposium on fluid power & motion control*, Sarasota, FL, 6–9 October 2013, pp.FPMC2013–4464. New York: ASME.
20. Baayoun MA, Daher N and Liermann M. Adaptive controller design of MRI compatible pneumatic teleoperation system. In: *Proceedings of the ASME/BATH 2015 symposium on fluid power & motion control*, Sarasota, FL, 6–9 October 2015, pp.FPMC2015–9567. New York: ASME.
21. ISO 6358. Pneumatic *fluid power—determination of flow-rate characteristics of components using compressible fluids*. Geneva: International Organization for Standardization, 2013.
22. Beater P. *Pneumatic drives: system design, modeling and control*. New York: Springer, 2007.
23. Krichel S and Sawodny O. Dynamic modeling of pneumatic transmission lines in Matlab/Simulink. In: *Proceedings of fluid power and mechatronics (FPM 2011) international conference*, Beijing, China, 17–20 August 2011, pp.24–29. New York: IEEE.
24. Astrom K and Wittenmark B. *Adaptive control*. Mineola, NY: Dover, 2008.
25. Astrom K and Wittenmark B. *Computer-controlled systems theory and design*. 3rd ed. Upper Saddle River, NJ: Prentice Hall, 1997.
26. Kucera V. Diophantine equations in control—a survey. *Automatica* 1993; 29(6): 1361–1375.

Appendix 1

State-space model parameters

The variables and parameters of the seventh-order linear state-space model before model reduction are listed here for reference. The equations include numerical values that correspond to conversion of units, which are listed in Table 1.

$$x_{mE} = \frac{l_{cyl}}{2}$$

$$P_{atm} = 1.013$$

$$P_{m1E} = \frac{-\sqrt{P_{atm}^2 b_v^2 - 2P_{atm}^2 b_v + 2P_{atm}^2 - 2P_{atm}P_s b_v^2 + 5P_s^2 b_v^2 - 6P_s^2 b_v + 2P_s^2)}}{2(b_v - 1)} - \frac{P_s b_v - P_{atm} b_v}{2(b_v - 1)}$$

$$P_{m2E} = P_{m1E}$$

$$x_{sE} = \frac{l_{cyl}}{2}$$

$$P_{s1E} = P_{m1E}$$

$$P_{s2E} = P_{m1E}$$

$$c_1 = \frac{RT}{V_{md} + x_{mE}\frac{A_p}{10^6}}$$

$$c_2 = \frac{P_{m1E}A_p}{10^6 V_{md} + x_{mE}A_p}$$

$$c_3 = \frac{RT}{V_{md} + (l_{cyl} - x_{mE})\frac{A_p}{10^6}}$$

$$c_4 = \frac{P_{m2E}A_p}{10^6 V_{md} + (l_{cyl} - x_{mE})A_p}$$

$$c_5 = \frac{RT}{V_{sd} + x_{sE}\frac{A_p}{10^6}}$$

$$c_6 = \frac{P_{s1E}A_p}{10^6 V_{sd} + x_{sE}A_p}$$

$$c_7 = \frac{RT}{V_{sd} + (l_{cyl} - x_{sE})\frac{A_p}{10^6}}$$

$$c_8 = \frac{P_{s2E}A_p}{10^6 V_{sd} + (l_{cyl} - x_{sE})A_p}$$

$$c_9 = C_v \rho_0 P_s \sqrt{1 - \left(\frac{\frac{P_{m1E}}{P_s} - b_v}{1 - b_v}\right)^2}$$

$$c_{10} = C_v \rho_0 P_s \sqrt{1 - \left(\frac{\frac{P_{m2E}}{P_s} - b_v}{1 - b_v}\right)^2}$$

$$c_{11} = \frac{100A_t}{L_t}$$

$$c_{12} = \frac{\frac{10^6 RT}{A_t}}{L_t}$$

$$c_{13} = \frac{32\mu \cdot 10^6}{\rho_0 D_t^2}$$